GEOPHYSICS, VOL. 78, NO. 5 (SEPTEMBER-OCTOBER 2013); P. D381–D392, 13 FIGS., 2 TABLES.
10.1190/GEO2013-0050.1

Mechanical properties of shale-gas reservoir rocks — Part 1: Static and dynamic elastic properties and anisotropy

Hiroki Sone[1] and Mark D. Zoback[2]

ABSTRACT

Understanding the controls on the elastic properties of reservoir rocks is crucial for exploration and successful production from hydrocarbon reservoirs. We studied the static and dynamic elastic properties of shale gas reservoir rocks from Barnett, Haynesville, Eagle Ford, and Fort St. John shales through laboratory experiments. The elastic properties of these rocks vary significantly between reservoirs (and within a reservoir) due to the wide variety of material composition and microstructures exhibited by these organic-rich shales. The static (Young's modulus) and dynamic (P- and S-wave moduli) elastic parameters generally decrease monotonically with the clay plus kerogen content. The variation of the elastic moduli can be explained in terms of the Voigt and Reuss limits predicted by end-member components. However, the elastic properties of the shales are strongly anisotropic and the degree of anisotropy was found to correlate with the amount of clay and organic content as well as the shale fabric. We also found that the first-loading static modulus was, on average, approximately 20% lower than the unloading/reloading static modulus. Because the unloading/reloading static modulus compares quite well to the dynamic modulus in the rocks studied, comparing static and dynamic moduli can vary considerably depending on which static modulus is used.

INTRODUCTION

Hydrocarbon production from unconventional shale-gas reservoirs has become common in the past decade, and there are increasing demands to understand the petrophysical and mechanical properties of these rocks. Generalized characterization of these organic-rich shales can be challenging because these rocks vary significantly. For example, formations in the Barnett Shale are known to be more silica rich, whereas Eagle Ford Shale rocks are generally carbonate rich containing relatively smaller amounts of silica and clays. In addition, shale gas reservoirs typically consist of many parasequence units, which create significant intrareservoir variations in lithology and petrophysical properties (Passey et al., 2010). Another source of complexity is their mechanical anisotropy. These rocks exhibit significant mechanical anisotropy due to the organized distribution of platy clay minerals (Hornby et al., 1994; Johnston and Christensen, 1995; Sondergeld and Rai, 2011) and compliant organic materials (Vernik and Nur, 1992; Vernik and Liu, 1997; Sondergeld et al., 2000; Vernik and Milovac, 2011). There are also indications that it is not only the amount of clay or organics, but also the maturity of the shales that may influence the anisotropy of these organic-rich shales (Vanorio et al., 2008; Ahmadov, 2011). Understanding the anisotropy and its causes is crucial because they strongly influence analyses/interpretations of seismic surveys, sonic logs, and microseismic monitoring.

Here, we report laboratory measurements on the elastic properties of core samples of shale-gas reservoir rocks collected from several different reservoirs in North America. We present data on the general mechanical behavior of these rocks, the static/dynamic elastic properties, and anisotropy to delineate the basic parameters that control gas-shale mechanical properties. We also discuss these data in the context of theoretical models to better understand how composition and fabric affect rock properties.

SAMPLE CHARACTERIZATION — COMPOSITION

Samples used in our experiments come from four different shale gas reservoirs: Barnett, Haynesville, Eagle Ford, and Fort St. John shales. Some basic reservoir and petrophysical information are summarized in Table 1 and Figure 1. The volumetric composition of all tested samples were determined by combining results from powder X-ray diffraction analysis and pyrolysis and by assuming a kerogen

Manuscript received by the Editor 12 February 2013; revised manuscript received 15 May 2013; published online 11 September 2013.
[1]Presently GFZ German Research Centre for Geosciences, Potsdam, Germany; formerly Stanford University, Department of Geophysics, Stanford, California, USA. E-mail: sone@gfz-potsdam.de.
[2]Stanford University, Department of Geophysics, Stanford, California, USA. E-mail: zoback@stanford.edu.

Table 1. Summary of reservoir conditions, material composition, and microstructural observations of the gas shale samples.

Sample group	In situ stress (MPa)	Maturity (Ro/Tmax) (% /°C)	Dry bulk density (g/cm^3)	QFP[3] (vol.%)	Carbonate (vol.%)	Clay (vol.%)	Kerogen (vol.%)	Estimated Porosity (%)	Description	Clay preferred orientation	Shape of organics[4]
Barnett-1	Sv, 65 Pp, 30 σ_{eff}, 35	Mature (oil to wet gas) Tmax = 445 – 465 Ro = 0.85 – 0.91	2.39–2.47	50–52	0–3	36–39	9–11	4–9	Silt grains in clayey matrix	Yes	Patches to lenses
Barnett-2			2.63–2.67	31–53	37–60	3–7	2–3	1–2	Carbonate rock	No	Very few patches
Haynesville-1	Sv, 85; Pp, 60–70 σ_{eff}, 15–25	Overmature (dry gas) Tmax = 525 – 545	2.49–2.51	32–35	20–22	36–39	8	6	Silt grains in clayey matrix	Yes	Lenses
Haynesville-2			2.60–2.62	23–24	49–53	20–22	4	3–4	Silt grains in clayey/ calcareous matrix	No	Lenses to layers
Eagle Ford-1	Sv, 90 Pp, 65 σ_{eff}, 25	Mature (wet gas) Ro = 1.29 – 1.39 Tmax = 478 – 481[5]	2.43–2.46	22–29	46–54	12–21	9–11	5–7	Calcareous biotic grains in clayey/ calcareous matrix	No	Lenses to layers
Eagle Ford-2			2.46–2.54	11–18	63–78	6–14	4–5	5–7	Calcareous biotic grains in clayey/ calcareous matrix	No	Lenses to layers
Fort St. John	Sv, 25–30 Pp, 10–12 σ_{eff}, 13–20	Mature (oil to wet gas) Tmax = 450 – 460	2.57–2.60	54–60	3–5	32–39	4–5	5–6	Silt grains in clayey matrix	Yes	Patches

[3]QFP: quartz, feldspar, pyrite.
[4]Shapes defined based on aspect ratio: patches, 0.5 ~ 1; lenses, 0.05 ~ 0.5; layers, <0.05.
[5]Average values of nearby samples.

density of 1.3 g/cm^3 (Mavko et al., 2009). Clay minerals in these rocks were mostly either illite or mixed layer illite-smectite (10%–25% expandability), with minor amounts of kaolinite and/or chlorite in some samples. Minerals such as apatite, marcasite, and barite were also identified, but they comprise less than a few percent of the whole rock volume. Porosity was estimated by comparing the dry bulk density and the average mineral densities (from X-ray diffraction) of the samples. Samples from Barnett, Haynesville, and Eagle Ford shales are further divided into two subgroups based on their mineralogy: subgroup 1 having more clay and kerogen volume compared with subgroup 2. Note that the compositions reflect some of the mineralogical characteristics of the reservoirs, but they do not necessarily represent the full spectrum of compositions found within each reservoir. We also report here a separate set of laboratory data, in the section, "Anisotropy data set," collected using Bossier/Haynesville shale samples. The rough compositional span of these samples is also shown in Figure 1, which provides an overview of the compositional variation within a single shale gas reservoir.

Figure 2a shows the kerogen volume plotted against the clay volume. When samples from a particular reservoir are compared (group 1 versus 2), there is a positive correlation between kerogen and clay volume, although there does not seem to be a universal trend representing all reservoirs. Porosity estimated based on the room-dry bulk density and average mineral density is also plotted against kerogen and clay volume in Figure 2b and 2c, respectively. These data are consistent with observations made by previous studies that the pore volume mainly reside within the solid organics and/or between the platy clay minerals in these gas shale rocks (Loucks et al., 2009; Curtis et al., 2010; Sondergeld et al., 2010). We cannot, however, differentiate which of the two constituents is carrying more pore volume than the other, because kerogen and clay volume correlate positively within a reservoir. Previous studies (Loucks et al., 2009; Curtis et al., 2010; Sondergeld et al., 2010) suggest that this depends on the particular reservoir.

SAMPLE CHARACTERIZATION — MICROSTRUCTURE

Optical microscope images of some representative samples used in the experiments are shown in Figure 3. The microstructures are mainly constructed of extremely fine grain clayey and/or calcareous matrix, silt-size detrital grains, biotic fragments, and solid organic materials of varying aspect ratios (α, defined as the short axis divided by the long axis). Barnett-2 samples, however, were an exception because they were dominated by large carbonate crystals with much less fine grain matrix components. At this scale, fabric anisotropy forming the bedding planes is defined by the combination of the following: preferred orientations of matrix clay, shape/orientation/distribution of organics, and alignment of elongated fossils. Aggregates of aligned clay minerals are always observed in the local scale in all samples when observed under the scanning electron microscope, but whether a preferred orientation of these clay aggregates persist at a larger scale is checked by observing the extinction/diagonal positions under the optical microscope with a cross-polarized light (Figure 3, Fort St. John shale images). Shapes of organics vary from nearly round patches ($\alpha = 0.5 - 1$) to thin layers ($\alpha < 0.05$), and they appear as strong sources of fabric anisotropy especially when the aspect ratio is low.

Observations from each sample group are also summarized in Table 1. In general, Eagle Ford samples and Haynesville-2 samples showed pronounced anisotropic fabric due to the low-aspect-ratio organics. On the other hand, organic materials in Barnett-1, Haynesville-1, and Fort St. John samples had higher aspect ratios, but they all exhibited preferred clay orientation. Comparison between the thin section observations and sample mineralogy (Figure 1) suggests that preferred clay orientation under the optical microscope vanishes when the clay volume is lower than about 30%. Loss of clay preferred orientation with increasing silt content has been known in sedimentary rocks (Gipson, 1966; Curtis et al., 1980), and we interpret that the clay fabric is losing its preferred orientation below some critical volume content, below which the framework of load-bearing grains dominates the rock fabric and disrupts the spatial continuity of the clay fabric. Vernik and Nur (1992) observe the texture of organic-rich Bakken shale samples and characterize it to be consisting of lenticular shale laminae imparted by a continuous network of organic matter. Since then, many authors have developed rock physics models of organic rich shales incorporating the texture and properties of the organic components (Vernik and Nur, 1992; Bandyopadhyay, 2009; Carcione et al., 2011). We did not observe this to be a general feature in our samples in which most organic matter appeared to be separated. This may be due to the limited kerogen volume present in our samples (0%–12%) compared with the shales studied by Vernik and Nur (1992) (0%–42%).

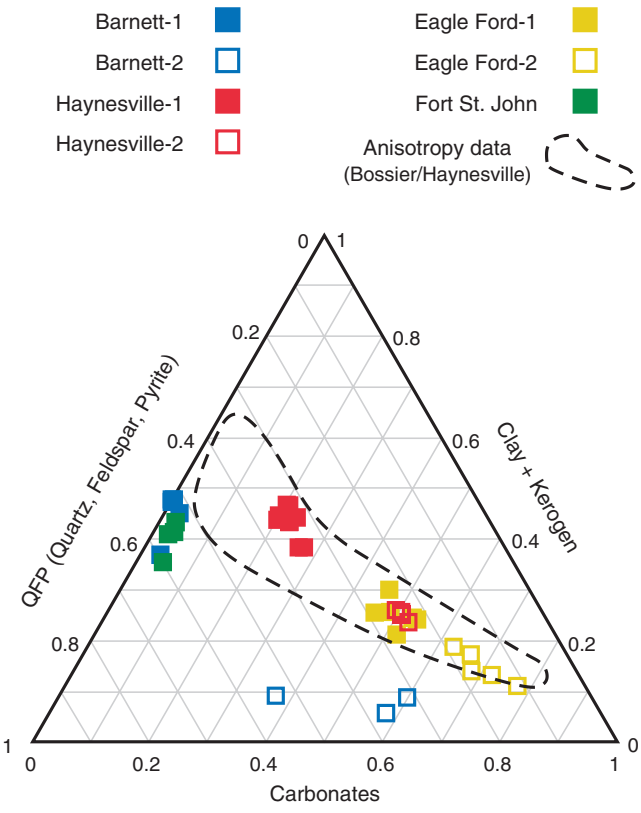

Figure 1. Ternary plot representation of the sample material composition.

LABORATORY PROCEDURE

Experiments were conducted in a servo-controlled triaxial apparatus, in which cylindrical samples of 1-in. diameter were deformed under hydrostatic and triaxial pressure condition with no pore pressure. The sample deformation in the axial and lateral direction was measured by displacement transducers to derive the static elastic properties, and ultrasonic P-wave and (fast) S-wave velocities parallel to the cylindrical axis were recorded at various times in the experiments to derive the dynamic elastic properties. Sone (2012) provides more details about the experimental setup and procedures. Samples were cored so that the cylindrical axes were either perpendicular or parallel to the bedding, hereafter referred to as vertical and horizontal samples, respectively. When both orientations were available, this allowed us to obtain some measures of the mechanical anisotropy. We treat the shale as a vertical transversely isotropic (VTI) medium with the x_3-axis being the axis of symmetry, so that the bedding normal and parallel P-wave moduli is represented by c_{33} and c_{11}, respectively, and the bedding normal and parallel (fast) S-wave moduli is represented by c_{44} and c_{66}, respectively.

In the experiments, first, the confining pressure ($P_{conf} = P_{axial}$) was first applied in several steps up to 10–60 MPa (hydrostatic stage, Figure 4a). Then differential stress ($P_{diff} = P_{axial} - P_{conf}$) was also applied in the axial direction in several steps, up to a stress below 50% of the ultimate rock strength (triaxial stage, Figure 4a) to ensure elastic behavior. Between each pressure step in the hydrostatic and triaxial stages, differential stress was kept constant for a sustained period of time (>3 h) to observe creep deformation, which is discussed in the companion paper (Sone and Zoback, 2013). Then the pressure was partially unloaded and reloaded before moving on to the next pressure step (Figure 4b). These procedures allowed us to obtain several measurements of dynamic and static elastic properties at different pressure levels and also check any hysteretic behavior of elastic properties from the differences between the *first-loading* and *unloading/reloading* static elastic constants. Finally, samples were taken to failure to measure intact and residual strengths (failure stage), which are also discussed in the companion paper. Detailed information on the pressure conditions in each experiment is provided in the appendices of Sone (2012).

All experiments were conducted under room-dry, room-temperature, and drained conditions. The Haynesville and Eagle Ford samples were sealed in wax after coring, but the Barnett and Fort St. John samples were not. Thus, the samples had been exposed to room humidity conditions for varying amounts of time. We did not attempt to actively control the pore fluid content. Injecting fluid in these extremely low permeability rocks in a controlled manner is not feasible and also introduces poroelastic effects. Removal of the residual fluids by drying the samples would take away the clay-bound water from the clay minerals; therefore, it would change the mechanical behavior of the rocks (Moore and Lockner, 2004). Hence, we chose to test the samples in "as-received" condition to best preserve the original hydration states of the clay minerals. We believe that the mechanical data were free of any poroelastic effects because of the low fluid saturation measured for some samples after core recovery (typically less than 40% including clay-bound water).

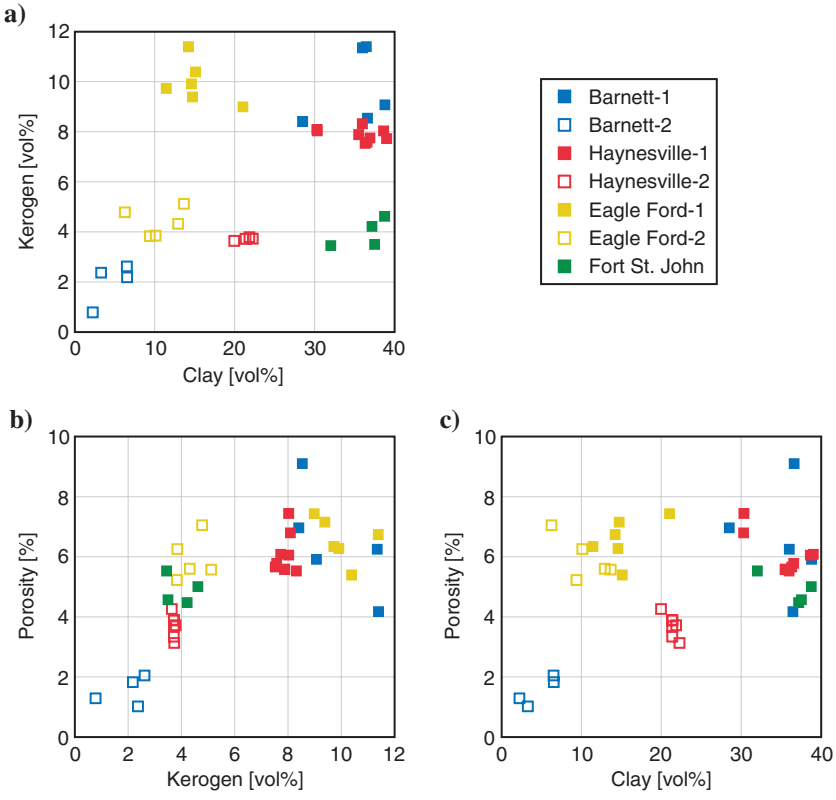

Figure 2. Relation between kerogen volume, clay volume, and porosity. (a) Kerogen volume versus clay volume. (b) Porosity versus kerogen volume. (c) Porosity versus clay volume.

ANISOTROPY DATA SET

As mentioned previously, we also report here a separate set of experimental data (anisotropy data set) collected elsewhere using Bossier/Haynesville samples. These samples were loaded axially at a constant strain rate of 10^{-5} s^{-1} under a constant confining pressure of 17.2 MPa (=2500 psi), during which the static and dynamic elastic constants were obtained from the stress-strain relation and ultrasonic velocity measurements, respectively. However, a set of 3 to 5 samples was cored from each depth so that the cylinder axes were angled at 0°, 30°, 45°, 60°, and 90° with respect to the bedding plane. This allowed the full characterization of the mechanical anisotropy of the VTI rocks, whereas the procedures described in the previous section only characterizes the difference between the bedding-parallel and bedding-perpendicular elastic properties.

Figure 5 shows an example of angle-dependent velocity data in the anisotropic data set conducted on a single group of samples from a particular depth in Haynesville shale. In a VTI medium, the P- and (fast) S-wave phase velocity changes with incidence angle (θ), measured from the symmetry axis (x_3), as in the following equations (Mavko et al., 2009):

$$V_p(\theta) = \sqrt{\frac{c_{11}\sin^2\theta + c_{33}\cos^2\theta + c_{44} + \sqrt{M}}{2\rho}}, \quad (1)$$

where $M = [(c_{11} - c_{44})\sin^2\theta + (c_{33} - c_{44})\cos^2\theta]^2 + (c_{13} + c_{44})^2 \sin^2 2\theta$;

$$V_{SH}(\theta) = \sqrt{\frac{c_{66}\sin^2\theta + c_{44}\cos^2\theta}{2\rho}}. \quad (2)$$

Equations 1 and 2 were fit to the θ-dependent velocity data by the least-squares method to obtain the best set of five stiffness constants (c_{11}, c_{33}, c_{44}, c_{66}, and c_{13}) that represent the samples from that depth. A total of 16 sets of velocity measurements similar to Figure 5 were analyzed in the anisotropy data set representing various lithofacies in the Bossier and Haynesville shales.

DEPENDENCE ON CLAY AND KEROGEN VOLUME

The elastic properties measured for each sample are plotted against the sum of clay and kerogen volume in Figure 6. Each panel plots the P-wave (c_{33}, c_{11}), S-wave (c_{44}, c_{66}), first-loading Young's modulus (E_3, E_1), and first-loading Poisson's ratio (v_{31}, v_{13}) data. Only one data point for each sample is shown, although multiple data points were collected from each sample at different pressure levels. We selected the data points shown when the P_{axial} was closest to 50 MPa, which represented a pressure level when most samples become free from pressure-stiffening effects due to the closure of soft pores such as cracks (see Appendix A). Data are plotted against the sum of clay and kerogen content because these are the anomalously compliant constituents of the rock and are expected to have the greatest influence on the overall properties.

In all modulus data (P-wave, S-wave, Young's modulus), we see an overall decreasing trend with increasing clay and kerogen volume. In all reservoirs, the low clay + kerogen subgroup 2 samples (open symbols) are stiffer than the subgroup 1 samples (filled symbols) reflecting the greater amount of stiff minerals (quartz and carbonates) and smaller amount of compliant materials (clay and organics) present in the subgroup 2 samples. However, the data scatter considerably about the overall trend especially seen by the relatively low moduli of the Eagle Ford samples despite their low clay and kerogen volume. We also confirm that there is significant anisotropy in all sample groups in which the horizontal samples (triangles) are much stiffer than the vertical samples (circles). However, the Barnett-2 sample exhibits no anisotropy reflecting its relatively isotropic fabric observed under the microscope (Figure 3).

For the static Poisson's ratio, it is difficult to make any inference about the dependence on sample composition. However, there seems to be a clear anisotropy in Poisson's ratio. Values of the horizontal Poisson's ratio, v_{13} (triangles), are generally larger compared with the vertical Poisson's ration, v_{31} (circles). This is consistent with the anisotropy observed in the Young's modulus (Figure 6c) because it follows from the symmetry of the elastic compliance tensor of a VTI medium that

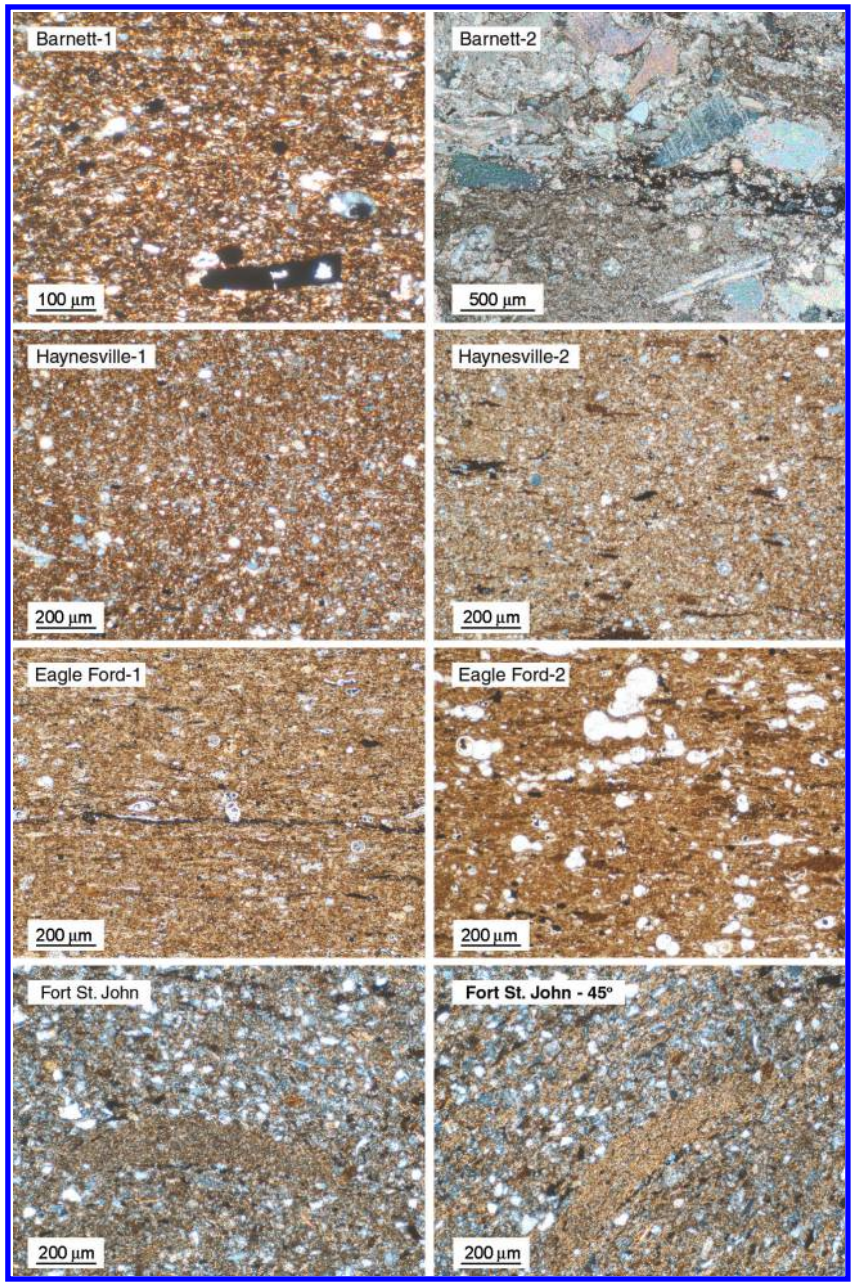

Figure 3. Thin section images of several representative samples used in the experiments. All images were taken under cross-polarized light. Two images of the Fort St. John show the extinction/diagonal positions at the same location to show where the oriented clays are distributed (bright-orange region in the diagonal position). All of the other images are oriented with the bedding direction from left to right.

$$\frac{\nu_{31}}{\nu_{13}} = \frac{E_3}{E_1}. \quad (3)$$

COMPARISON WITH THEORETICAL BOUNDS

To understand the variability of elastic properties observed in the laboratory, we also compare the data with some theoretical bounds. The bounds were constructed by considering gas shales as binary mixtures of "soft" and "stiff" end-member components, where the soft component represents the clay and kerogen and the stiff component represents the rest of the constituents dominated mostly by quartz and calcite. Elastic properties of the soft and stiff components were each approximated by taking the Hill's average (Mavko et al., 2009) of isotropic quartz/calcite and clay/kerogen properties, respectively, as shown in Table 2. Then, based on the end-member properties, the theoretical upper and lower bounds were determined by calculating the Voigt and Reuss averages of the end-member components (Figure 6). Note that we ignored the effect of porosity in this simplified shale model because porosity is rather small and the pore compliance is mostly accounted for a priori in the elastic properties of the soft components. Porosity in these shales is concentrated in the soft component volume because the clays and kerogen in gas shales contain pore spaces down to the nanoscale (Loucks et al., 2009; Curtis et al., 2010; Sondergeld et al., 2010) usually nonresolvable by mechanical testing. Thus, the measurements and estimates of their elastic properties that we reference in Table 2 (Vanorio et al., 2003; Bandyopadhyay, 2009) likely reflect their properties as a porous material.

The laboratory data generally conform to the theory and lie within the Voigt and Reuss bounds. However, the static Young's modulus data are distributed slightly lower than predicted by the theoretical bounds. We suggest that the discrepancy mainly reflects the difference between dynamic and static properties, specifically in the soft components. The soft-component properties reference in Table 2 were estimated based on laboratory dynamic measurements, but these relatively porous components should undergo more inelastic deformation during large-strain static loading, thus appearing more compliant. In Figure 6c, another pair of theoretical bounds is drawn with the soft-component static Young's modulus (Figure 6c, dashed curves) lowered to half of its original value. Such manipulation successfully shifts the upper and lower bounds so that the bounds better capture the range of Young's modulus values observed. The shale model still oversimplifies the variability of shales despite the first-order success of this simplified shale model in capturing the scatter of elastic properties. For instance, stiff and soft end members do not necessarily contain an equal amount of clay and kerogen or quartz and calcite as assumed in Table 2. Quartz tends to be most abundant in Barnett Shale samples, whereas calcite tends to be more abundant in Eagle Ford samples. Also, some pore space may also reside within and between the stiff components (Curtis et al., 2010; Sondergeld et al., 2010), for instance, within the calcite, depending on the type of calcite depositions. Nevertheless, the simple shale model seems to generally describe the variability of gas shale elastic properties.

From the comparison of the data with the theoretical bounds, the anomalously low moduli values of the Eagle Ford samples (despite their low clay and kerogen volume) could be interpreted to be the consequence of their extreme fabric anisotropy. Voigt and Reuss averages correspond to the most extreme case of anisotropy represented by a completely layered rock. Thus, the fact that the Eagle Ford vertical data lies on the Reuss average prediction suggests that the fabric anisotropy is strong in Eagle Ford samples. This inference is consistent with our microstructural observations

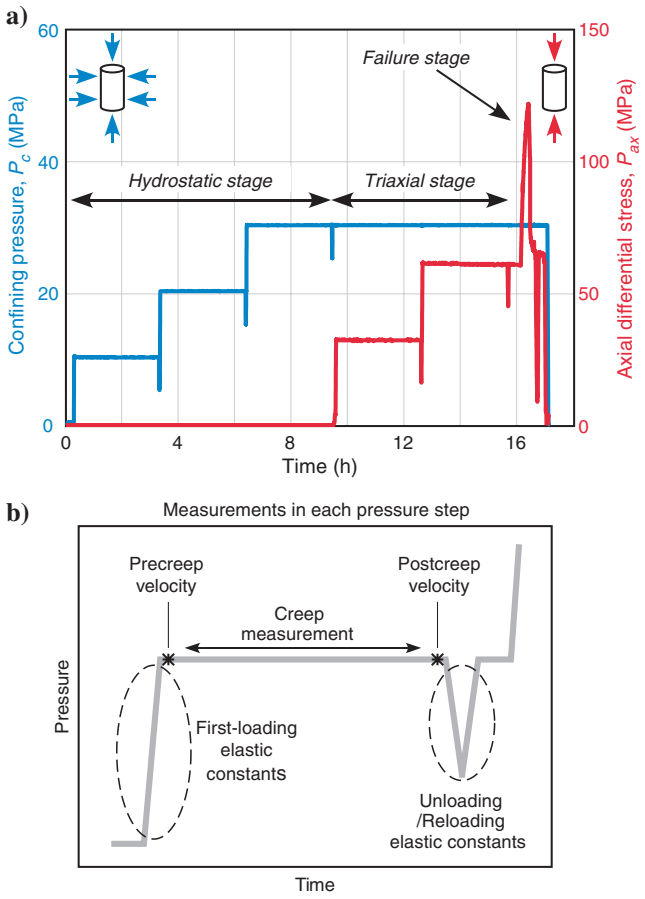

Figure 4. (a) The pressure-time history during an experiment. (b) Schematic showing the timing of each mechanical property measurement during a single pressure step. The gray curve represents pressure as a function of time.

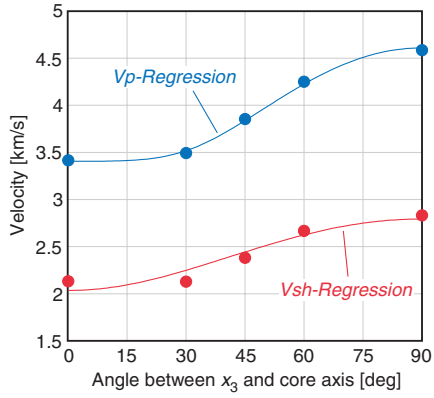

Figure 5. Example of a set of velocity measurement conducted in the anisotropy data set for a Bossier/Haynesville sample at a confining pressure of 17.2 MPa.exhibits no anisotropy reflecting its relatively

(Figure 3, Table 1) that organic materials in the Eagle Ford sample show the lowest aspect ratio out of all the samples.

MECHANICAL ANISOTROPY

In this section, we present data on mechanical anisotropy of the gas shales determined from the laboratory results. Anisotropy parameters such as ε, γ (Thomsen, 1986), and the ratio of horizontal to vertical Young's modulus E_h/E_v for each sample group were calculated by comparing the averages of vertical and horizontal stiffness within each sample group (except for the Fort St. John Shales). Taking advantage of the full set of five stiffness constants obtained from the anisotropy data set, the Thomsen parameter δ was also obtained for the Haynesville/Bossier shale samples in the anisotropy data set.

Figure 7 shows the degree of anisotropy plotted against the sum of clay and kerogen volume in the samples for dynamic and static moduli data. We see from the data that mechanical anisotropy increases with soft component volume consistent with previous studies. Elastic anisotropy of shales is understood to be the result of the anisotropic fabric created by the preferred orientation of platy clay minerals and the anisotropic elastic properties of the clay minerals itself. Previous studies have also emphasized that the bulk rock anisotropy is influenced by the amount of organic content in the rock (Vernik and Nur, 1992; Vernik and Liu, 1997). Solid organic materials are anomalously compliant compared with the surrounding minerals (Ahmadov et al., 2009; Kumar et al., 2012), and if their shape or distribution is anisotropic, they can become strong sources of mechanical anisotropy. In our data set, it is difficult to distinguish the effect of clay and kerogen on the bulk rock anisotropy given that clay and kerogen volume tend to have a positive correlation in our samples (Figure 2a).

We also compare the degree of anisotropy with the vertical velocities because previous studies have reported correlations between them in shales (Tsuneyama and Mavko, 2005; Bandyopadhyay, 2009). A strong correlation is also found in our data set, which is insensitive to the reservoir locality and possibly suggests a universal trend (Figure 8). Qualitatively, this trend is understood to be the simultaneous effect of clay and kerogen to lower the overall velocity and enhance mechanical anisotropy. When our results are compared with data from organic-rich shales in Vernik and Liu (1997) (Figure 8, gray crosses), we find that our gas shale data tend to distribute toward the higher-anisotropy side of their data set showing a much confined trend. This was somewhat contrary to our expectations because our samples have less kerogen volume (0%–12%) compared with those studied in Vernik and Liu (1997) (0%–42%), and anisotropy is expected to increase with kerogen volume. Further microstructural examination and modeling are required to understand this apparently confined trend, but one possibility is that the relatively high anisotropy is related to the narrow range of maturity exhibited by our gas shale samples. By comparing the degree of anisotropy to the sample maturity (R_o) in the data set from Vernik and Liu (1997), Vanorio et al. (2008) argue that organic-rich shales may exhibit the highest degree

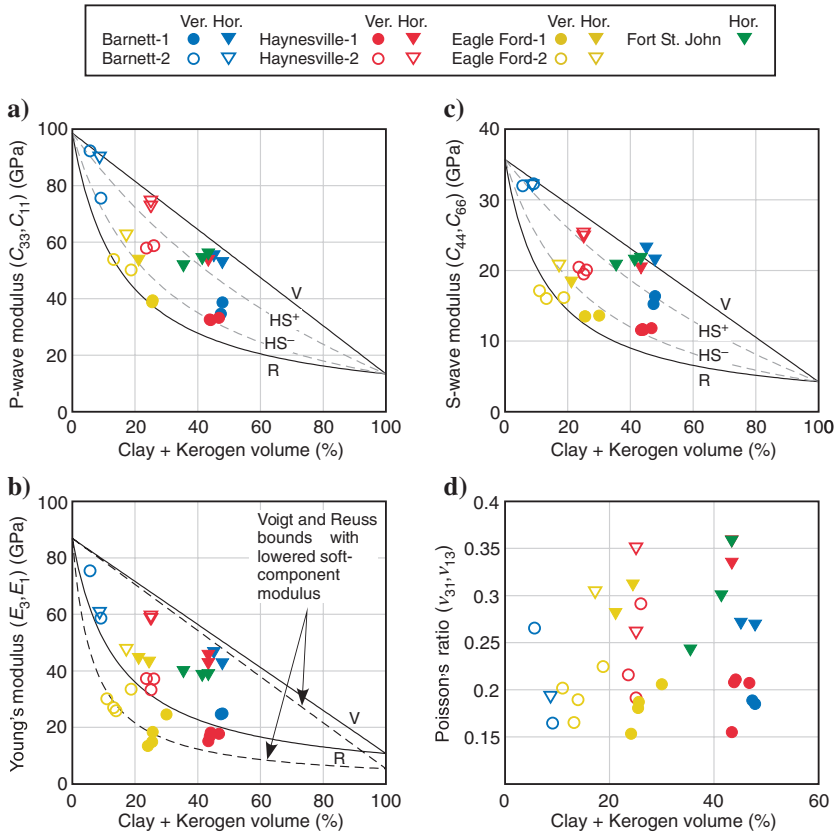

Figure 6. Dynamic and static moduli data plotted against the sum of clay and kerogen volume compared with Voigt/Reuss bounds and upper/lower Hashin-Shtrikman bounds. (a) P-wave modulus. (b) S-wave modulus. (c) Static Young's modulus. (d) Static Poisson's ratio. The Voigt and Reuss bounds were calculated using values from Table 2. In (c), the dashed curves represent the Voigt and Reuss bound drawn by lowering the soft-component Young's modulus to half of its original value shown in Table 2.

Table 2. Elastic properties used to calculate the upper and lower bounds in Figure 6.

	K (GPa)	μ (GPa)	M (GPa)	E (GPa)
Quartz (Mavko et al., 2009)	37	44	—	—
Calcite (Mavko et al., 2009)	70.2	29	—	—
"Stiff" component[6]	51	35.7	98.6	86.9
Clay (Vanorio et al., 2003)	12	6	—	—
Kerogen (Bandyopadhyay, 2009)	5	3	—	—
"Soft" component[6]	7.8	4.3	13.4	10.8

[6]Stiff and soft component properties are the Hill's average (50% mixtures) of quarts/calcite and clay/kerogen, respectively.

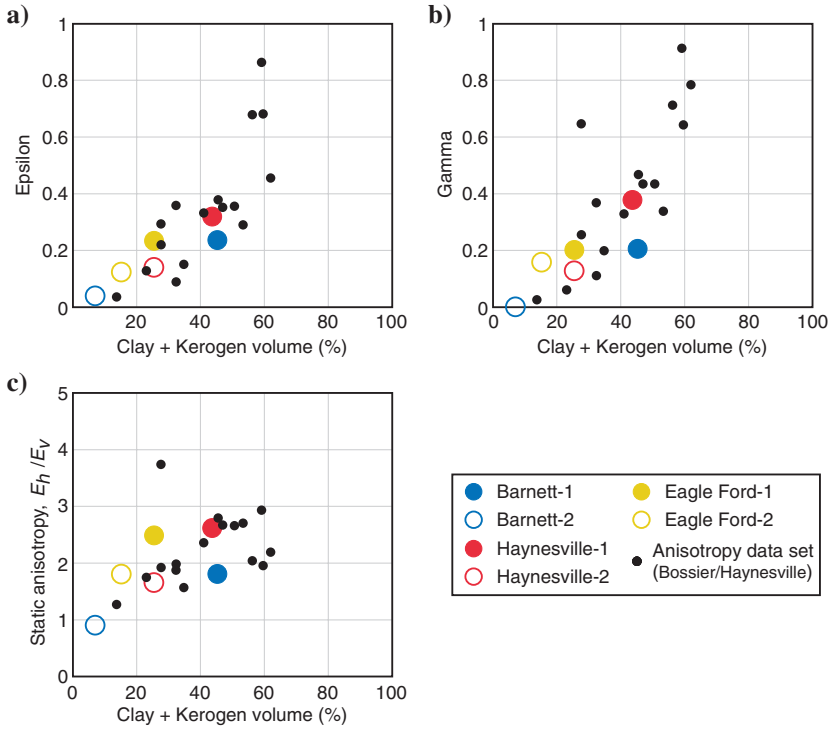

Figure 7. Comparison of anisotropy parameters with the sum of clay and kerogen volume. (a) Epsilon. (b) Gamma. (c) Young's modulus anisotropy.

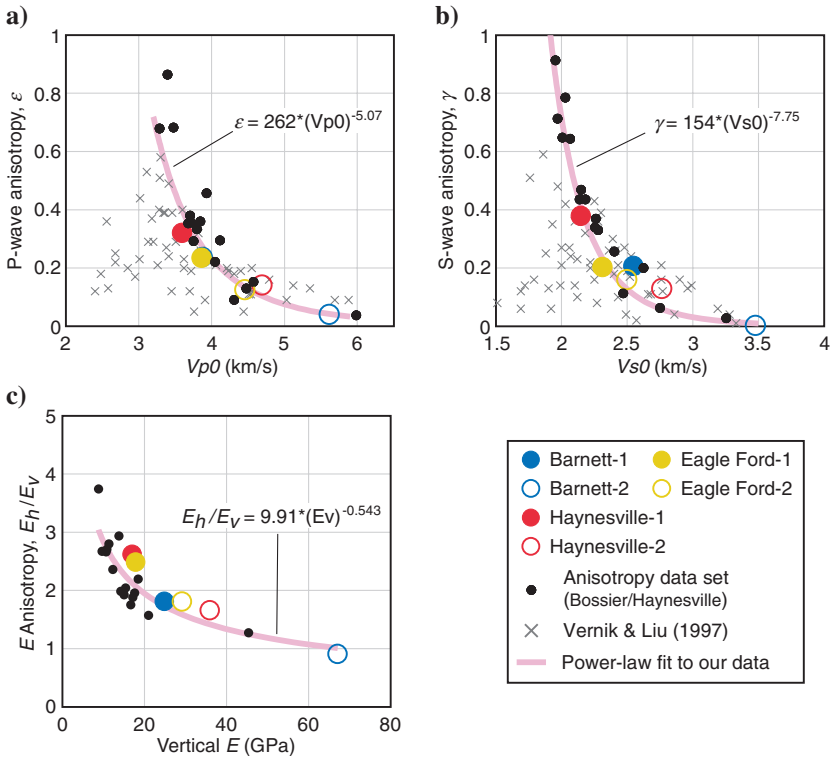

Figure 8. Comparison of anisotropy parameters with vertical velocity (V_P0, V_S0) and vertical modulus. (a) Epsilon versus vertical P-wave velocity. (b) Gamma versus vertical S-wave velocity. (c) E_h/E_v versus E_v. Gray crosses are data from Vernik and Liu (1997). Magenta curves represent the least-squares fit of a power-law equation to our laboratory data.

of anisotropy at around the peak maturity ($R_o \sim 0.6 - 1.3$) due to microcrack alignment and kerogen distribution. Ahmadov (2011) also suggests the evolution of the spatial distribution of kerogen with maturity based on microfabric observations of mature and postmature Bakken shales, such that the bedding parallel kerogen in the mature shales becomes finely scattered in the postmature shales. The organic-rich shales in Vernik and Liu (1997) span maturation levels from immature to postmature organic-rich shales, whereas the gas shales we studied come from mature shale reservoirs. This may explain why we see a confined trend between the degree of anisotropy and vertical velocity for gas shales.

We compare the Thomsen anisotropy parameters ε, γ, and δ in Figure 9. As past studies have observed, epsilon and gamma nearly have a one-to-one correlation with the exception of a few samples. The range of values we obtain for delta is similar to those that Vernik and Liu (1997) and Sondergeld et al. (2000) report. However, we do not see any strong correlation of delta with the other anisotropy parameters, again consistent with previous studies (Thomsen, 1986; Vernik and Liu, 1997). Whether this is due to measurement error, sample variability, or the intrinsic property of the rock is unclear.

STATIC-DYNAMIC RELATIONS

Before discussing the relationship between static and dynamic rock properties, we compare the static elastic constants measured during the first time axial differential stress was applied (first-loading) and also during the partial unloading and reloading of the axial differential stress (unloading/reloading) (Figure 4). The Young's modulus and the Poisson's ratio measured at these two different timings are compared in Figure 10. Measurements from all pressure steps and all samples are plotted in Figure 10. We find from the comparison that the Young's modulus is consistently lower during first-loading compared to the Young's modulus during unloading/reloading. Although there is some scatter in the correlation, on average, the first-loading Young's modulus is about 20% lower than the unloading/reloading. On the other hand, comparison between the first-loading and unloading/reloading Poisson's ratio does not yield a clear relation between them. On average, the first-loading Poisson's ratio may seem to be lower than the unloading/reloading Poisson's ratio, but the scatter in the data is wide and does not permit a conclusive observation.

The difference between the first-loading and unloading/reloading static Young's modulus found in Figure 10a poses the question of which static moduli is more appropriate in discussing

the static reservoir deformation needed for production forecasting and assessment of production-related stress changes. The difference between the first-loading and unloading/reloading properties is a well-known hysteresis effect seen in soil/rock mechanics caused by inelastic deformation, and the stress level at which the hysteresis effect starts to appear is typically regarded as the memory of the maximum stress experienced by the rock. However, the difference in first-loading and unloading/reloading modulus was observed at all pressure steps above and below the in situ effective stress levels. Thus, the laboratory results suggest that the shale samples have lost their "memory" due to some decompaction process. One possibility is that overpressured gas has expanded the pore spaces during recovery of the core. Also, core material is known to gradually expand over time, a phenomenon known as *anelastic strain recovery* (Blanton, 1983; Warpinski and Teufel, 1986). Another possibility is that pore pressure was actually higher than given in Table 2, for instance close to the overburden pressure, so the sample behaviors are actually reflecting the very low in situ effective stress close to zero. Although the exact contribution of these processes is not understood, the persistent hysteretic behavior of the gas shale samples alerts us to carefully consider which laboratory data, first-loading or unloading/reloading, is more relevant to the problem of interest.

Figure 11 shows the two static-dynamic relations derived from our data using first-loading and unloading/reloading static Young's moduli. The dynamic Young's modulus was approximated by applying the following isotropic equations to the measured P- and S-wave modulus:

$$E_1^{\text{apparent}} = \frac{c_{66}(3c_{11} - 4c_{66})}{c_{11} - c_{66}},$$
$$E_3^{\text{apparent}} = \frac{c_{44}(3c_{33} - 4c_{44})}{c_{33} - c_{44}}. \quad (4)$$

The use of this equation is not precisely correct for a VTI medium, but we find that the error of using these isotropic equations rather than the complete anisotropic equations was small (see Appendix B). Figure 11 shows that the first-loading static modulus is consistently lower than the dynamic modulus, in agreement with many static-dynamic relations published to date (Mavko et al., 2009). This is the consequence of the additional inelastic deformation captured in the static modulus measurements. However, the unloading/reloading static modulus plots around the one-to-one correspondence line, indicating that most of the inelastic deformation captured in the first-

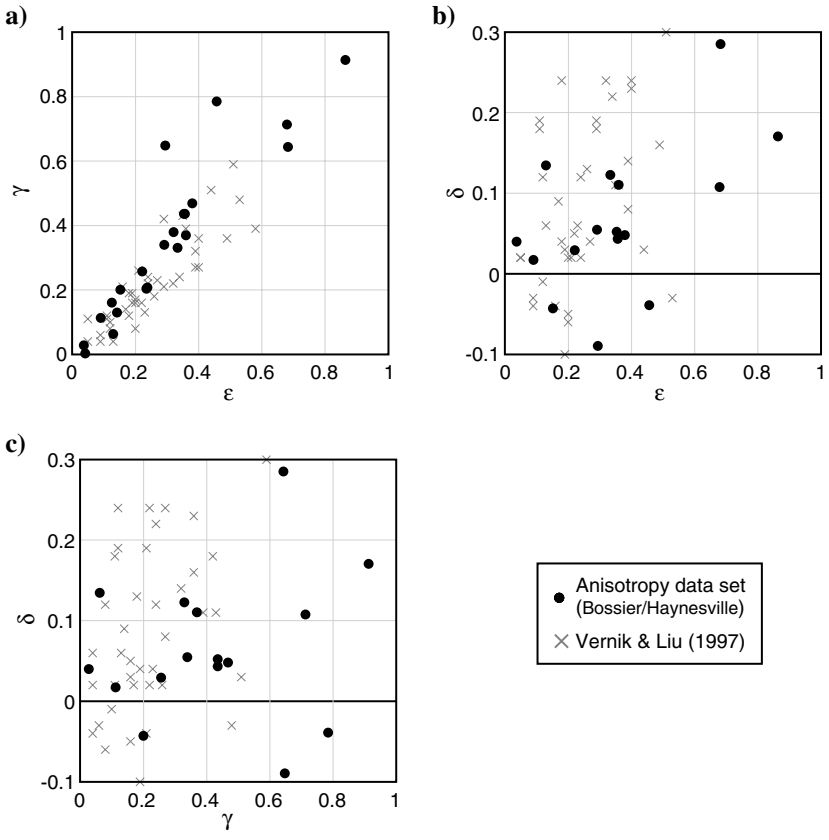

Figure 9. Comparison between Thomsen anisotropy parameters. (a) Epsilon versus gamma. (b) Epsilon versus delta. (c) Gamma versus delta. Gray crosses are data from Vernik and Liu (1997).

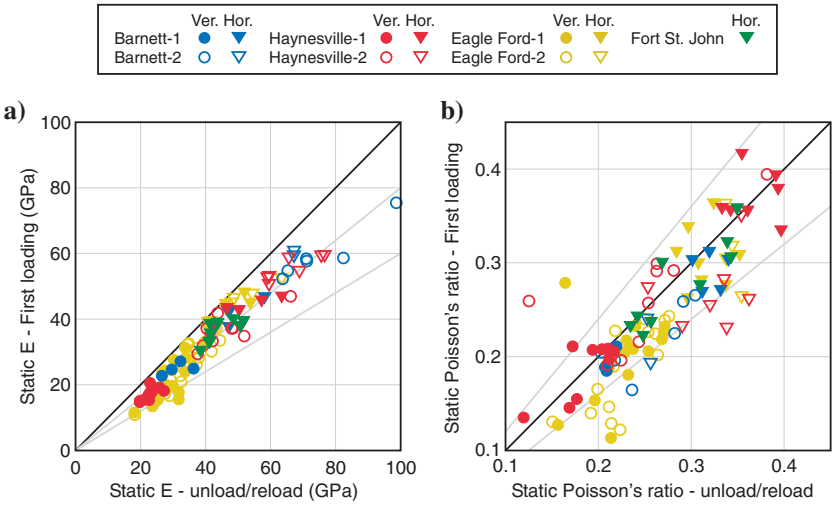

Figure 10. Comparison between first-loading and unloading/reloading elastic properties. (a) Comparison of static Young's modulus. The black line indicates one-to-one correspondence. The two gray lines indicate 20% and 40% differences. (b) Comparison of static Poisson's ratio. The black line indicates one-to-one correspondence. The two gray lines indicated 20% differences.

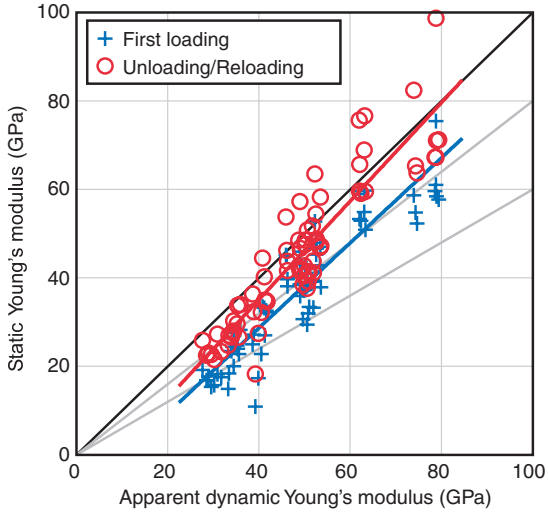

Figure 11. Static versus dynamic relation for the Young's modulus derived from experimental data using first-loading and unloading/reloading static modulus. The vertical and horizontal Young's moduli are plotted. The black solid line represents one-to-one correspondence, and the two gray lines represent a 20% and a 40% difference. The apparent dynamic Young's modulus is defined by equation 4. Blue and red lines are linear fits to the first-loading and unloading/reloading data, respectively.

loading static measurements was not recoverable during the laboratory time scale (~hours).

This suggests that static modulus estimated from static-dynamic relations can vary by up to 20%–30% depending on which static modulus, first-loading or unloading/reloading, is used. During shale gas completion and production, these reservoirs undergo drastic changes in stress states as pore pressure is locally raised close to the overburden stress during hydraulic fracturing, then drawn down below the initial pore pressure as hydrocarbon is produced. Therefore, the static elastic moduli of the reservoir rocks may take different values depending on the stage of development. Most published static-dynamic relations do not specify how the static moduli were measured. However, it may be important to distinguish and carefully select between the two static moduli when one uses static-dynamic relations to analyze deformation of shale-gas reservoirs.

CONCLUSIONS

Our laboratory results show the wide variation of elastic mechanical properties of shale-gas reservoir rocks between reservoirs and within a reservoir. As expected from basic rock physics principles, the elastic properties of these rocks are a strong function of their material composition. As the microstructural observations suggested, some gas shales exhibit an extremely high degree of fabric anisotropy, whereas some do not exhibit any fabric anisotropy. This is reflected in the laboratory data and thus causes the elastic properties to scatter widely between the upper and lower theoretical bounds expected from their compositions. Thus, shale elastic properties are a strong function of composition and fabric anisotropy. The anisotropy of the gas shale samples, described by Thomsen parameters, was found to increase with clay and organic content. The anisotropy was also found to correlate strongly with the vertical velocities and modulus. These trends are consistent with past findings. Comparison of our data with other organic-rich shale data shows that the anisotropy is relatively high in the studied gas shale samples despite their relatively low organic content. We suggest that the higher anisotropy observed in our samples is related to the difference in the range of maturity of the samples.

We also observed persistent differences in the static modulus measured during first-loading and unloading/reloading regardless of whether the stress level was above or below the in situ effective stress level, which speaks to the difficulty in recovering the in situ static elastic properties in the lab. The differences in the two types of elastic modulus suggest that static moduli estimated from static-dynamic relations can vary by as much as 20%–30% depending on the choice of static modulus between the first-loading and unloading/reloading. We suggest that first-loading and unloading/reloading static elastic properties are collected to better constrain the static reservoir mechanical behavior during shale gas development.

ACKNOWLEDGMENTS

We thank BP, ConocoPhillips, and Unconventional Gas Resources for providing us with the core samples and data necessary to carry out this research. We also thank the reviewers for their constructive comments. Financial support was provided by the Stanford Rock Physics and Borehole Geophysics (SRB) Industrial Consortium, Chevron, and ConocoPhillips.

APPENDIX A

PRESSURE DEPENDENCE OF THE DYNAMIC ELASTIC MODULI

The measured elastic moduli exhibited pressure dependence. The change in moduli with pressure is generally easier to track in the dynamic moduli data because dynamic measurements only require small elastic strains, whereas static measurements involve large strains including significant nonlinear inelastic strains. Figure A-1 shows dynamic moduli data plotted against total axial pressure, the sum of confining and axial differential pressure. We see from the data that most samples lose their pressure dependence above about 50 MPa axial pressure.

APPENDIX B

APPROXIMATING DYNAMIC YOUNG'S MODULUS IN VTI MEDIUM USING ISOTROPIC EQUATIONS

For an isotropic medium, the dynamic Young's modulus is determined precisely from the P- and S-wave moduli by the following equation:

$$E = \frac{\mu(3M - 4\mu)}{M - \mu}. \tag{B-1}$$

For a VTI medium, as in horizontally layered shales, equations relating the Young's modulus and the stiffness constants depend on the orientation and involve four independent stiffness constants as shown below:

$$E_{\text{vertical}} = E_3 = c_{33} - \frac{2c_{13}^2}{c_{11}+c_{12}}$$

$$E_{\text{horizontal}} = E_1 = c_{11} + \frac{c_{13}^2(-2c_{11}+c_{12}) + c_{12}(-c_{33}c_{12}+c_{13}^2)}{c_{33}c_{11}-c_{13}^2}. \quad \text{(B-2)}$$

However, this equation is usually not practical for many laboratory data because the stiffness constant c_{13} is not determined due to limited sample availability.

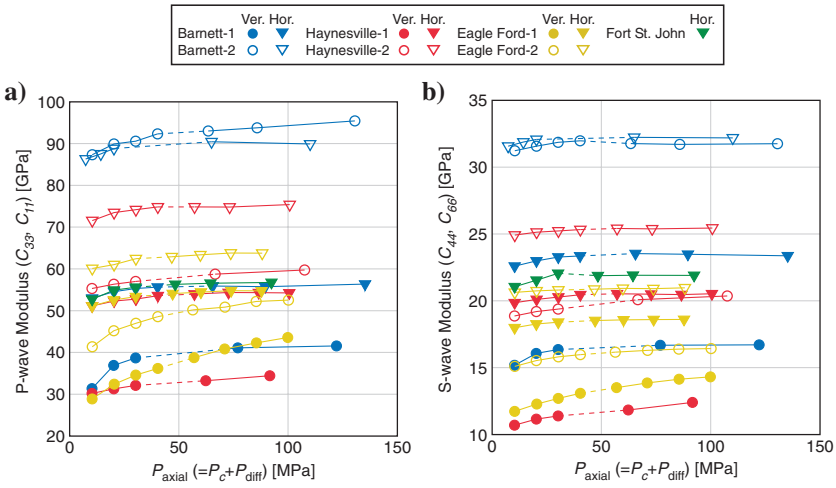

Figure A-1. Pressure dependence of the dynamic moduli. (a) P-wave modulus data plotted against axial pressure (sum of confining pressure and axial differential stress). (b) S-wave modulus data plotted against axial pressure. Data from the hydrostatic and triaxial stages are connected by dotted lines. Circles represent vertical samples, and triangles represent horizontal samples. Filled symbols represent subgroup-1 samples with more clay and organic content compared with the subgroup-2 samples (open symbols).

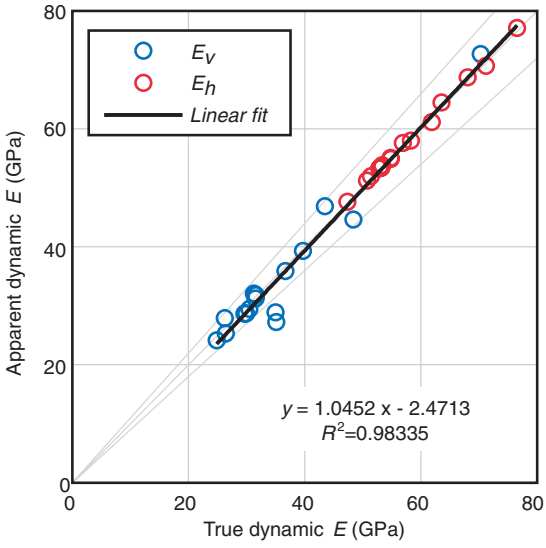

Figure B-1. Apparent dynamic Young's modulus versus true dynamic Young's modulus. The gray lines show one-to-one correspondence and 10% differences. The black line is a linear fit to the data (equation shown inside the panel).

Using the anisotropy data set that contains complete sets of stiffness constants for 16 different samples, we evaluated the error of using equation B-1 to calculate the apparent dynamic Young's modulus rather than using equation B-2 to calculate the true dynamic Young's modulus in a VTI medium. Figure B-1 shows the apparent dynamic Young's modulus against the true dynamic Young's modulus for the vertical and horizontal directions. The plot shows a good agreement between each other. With the exception of several vertical samples, the agreement is within 5%. Although this is what we find for just the Bossier/Haynesville shales in the data set, we judged that it is reasonable to expect a similar agreement for the other shale samples that we used in our experiment and used the apparent dynamic Young's modulus to discuss the static-dynamic relations in Figure 11.

REFERENCES

Ahmadov, R., 2011, Micro-textural, elastic and transport properties of source rocks: Ph.D. thesis, Stanford University.

Ahmadov, R., T. Vanorio, and G. Mavko, 2009, Confocal laser scanning and atomic-force microscopy in estimation of elastic properties of the organic-rich Bazhenov Formation: The Leading Edge, **28**, 18–23, doi: 10.1190/1.3064141.

Bandyopadhyay, K., 2009, Seismic anisotropy: Geological causes and its implications to reservoir geophysics: Ph.D. thesis, Stanford University.

Blanton, T. L., 1983, The relation between recovery deformation and in situ stress magnitudes: Presented at SPE/DOE Symposium on Low Permeability Gas Reservoirs, SPE 11624.

Carcione, J. M., H. B. Helle, and P. Avseth, 2011, Source-rock seismic-velocity models: Gassmann versus Backus: Geophysics, **76**, no. 5, N37–N45, doi: 10.1190/geo2010-0258.1.

Curtis, C. D., S. R. Lipshie, G. Oertel, and M. J. Pearson, 1980, Clay orientation in some Upper Carboniferous mudrocks, its relationship to quartz content and some inferences about fissility, porosity and compactional history: Sedimentology, **27**, 333–339, doi: 10.1111/j.1365-3091.1980.tb01183.x.

Curtis, M. E., R. J. Ambrose, C. H. Sondergeld, and C. S. Rai, 2010, Structural characterization of gas shales on the micro- and nano-scales: Presented at Canadian Unconventional Resources & International Petroleum Conference, CUSG/SPE 137693.

Gipson, M., 1966, A study of the relations with depth, porosity and clay-mineral orientation in Pennsylvanian Shales: Journal of Sedimentary Petrology, **36**, 888–903, doi: 10.2110/jsr.36.1143.

Hornby, B. E., L. M. Schwartz, and J. A. Hudson, 1994, Anisotropic effective-medium modeling of the elastic properties of shales: Geophysics, **59**, 1570–1583, doi: 10.1190/1.1443546.

Johnston, J. E., and N. I. Christensen, 1995, Seismic anisotropy of shales: Journal of Geophysical Research, **100**, 5991–6003, doi: 10.1029/95JB00031.

Kumar, V., C. H. Sondergeld, and C. S. Rai, 2012, Nano to macro mechanical characterization of shale: Presented at SPE Annual Technical Conference and Exhibition, SPE 159804.

Loucks, R. G., R. M. Reed, S. C. Ruppel, and D. M. Jarvie, 2009, Morphology, genesis, and distribution of nanometer-scale pores in siliceous mudstones of the Mississippian Barnett Shale: Journal of Sedimentary Research, **79**, 848–861, doi: 10.2110/jsr.2009.092.

Mavko, G., T. Mukerji, and J. Dvorkin, 2009, The rock physics handbook, 2nd ed.: Cambridge University Press.

Moore, D. E., and D. A. Lockner, 2004, Crystallographic controls on the frictional behavior of dry and water-saturated sheet structure minerals: Journal of Geophysical Research, **109**, B03401, doi: 10.1029/2003JB002582.

Passey, Q. R., K. M. Bohacs, W. L. Esch, R. Klimentidis, and S. Sinha, 2010, From oil-prone source rocks to gas-producing shale reservoir — Geologic and petrophysical characterization of unconventional shale-gas reservoir: Presented at CPS/SPE International Oil & Gas Conference and Exhibition, SPE 131350.

Sondergeld, C. H., R. J. Ambrose, C. S. Rai, and J. Moncrieff, 2010, Microstructural studies of gas shales: Presented at SPE Unconventional Gas Conference, SPE 131771.

Sondergeld, C. H., and C. S. Rai, 2011, Elastic anisotropy of shales: The Leading Edge, **30**, 324–331, doi: 10.1190/1.3567264.

Sondergeld, C. H., C. S. Rai, R. W. Margesson, and K. J. Whidden, 2000, Ultrasonic measurement of anisotropy on the Kimmeridge shale: 70th Annual International Meeting, SEG, Expanded Abstracts, 1858–1861.

Sone, H., 2012, Mechanical properties of shale gas reservoir rocks and its relation to the in-situ stress variation observed in shale gas reservoirs: Ph.D. thesis, Stanford University.

Sone, H., and M. D. Zoback, 2013, Mechanical properties of shale gas reservoir rocks — Part 2: Ductile creep, brittle strength, and their relation to the elastic modulus: Geophysics, **78**, this issue, doi: 10.1190/geo2013-0051.1.

Thomsen, L., 1986, Weak elastic anisotropy: Geophysics, **51**, 1954–1966, doi: 10.1190/1.1442051.

Tsuneyama, F., and G. Mavko, 2005, Velocity anisotropy estimation for brine-saturated sandstone and shale: The Leading Edge, **24**, 882–888, doi: 10.1190/1.2056371.

Vanorio, T., T. Mukerji, and G. Mavko, 2008, Emerging methodologies to characterize the rock physics properties of organic-rich shales: The Leading Edge, **27**, 780–787, doi: 10.1190/1.2944163.

Vanorio, T., M. Prasad, and A. Nur, 2003, Elastic properties of dry clay mineral aggregates, suspensions and sandstones: Geophysical Journal International, **155**, 319–326, doi: 10.1046/j.1365-246X.2003.02046.x.

Vernik, L., and X. Liu, 1997, Velocity anisotropy in shales: A petrophyscial study: Geophysics, **62**, 521–532, doi: 10.1190/1.1444162.

Vernik, L., and J. Milovac, 2011, Rock physics of organic shales: The Leading Edge, **30**, 318–323, doi: 10.1190/1.3567263.

Vernik, L., and A. Nur, 1992, Ultrasonic velocity and anisotropy of hydrocarbon source rocks: Geophysics, **57**, 727–735, doi: 10.1190/1.1443286.

Warpinski, N. R., and L. W. Teufel, 1986, A viscoelastic constitutive model for determining in situ stress magnitudes from anelastic strain recovery of core: Presented at SPE 61st Annual Technical Conference and Exhibition, SPE 15368.